Construction and Building Materials 154 (2017) 1234–1249

Contents lists available at ScienceDirect

Construction and Building Materials

journal homepage: www.elsevier.com/locate/conbuildmat

Virtual Special Issue
Ground-Penetrating Radar and Complementary
Non-Destructive Testing Techniques in Civil Engineering

High-resolution investigation of masonry samples through GPR and electrical resistivity tomography

Giorgio De Donno *, Luca Di Giambattista, Luciana Orlando

"Sapienza" University of Rome, DICEA Via Eudossiana, 18, 00184 Rome, Italy

HIGHLIGHTS

- We use GPR and ERT for the characterization of masonry samples.
- We add a dielectric material for improving the GPR antenna-sample coupling.
- GPR data are analysed in non-conventional mode.
- We are able to detect fractures and weakness zones caused by the load application.

ARTICLE INFO

Article history:
Received 13 December 2016
Received in revised form 27 April 2017
Accepted 17 June 2017
Available online 24 June 2017

Keywords:
Geophysics
Masonry samples
Ground penetrating radar
Electrical resistivity tomography
Fractured zone
Static load test

ABSTRACT

This paper aims to explore potential and limits of the combined use of ground penetrating radar (GPR) and electrical resistivity tomography (ERT) investigations for the characterization of reinforced masonry samples. To this aim, both techniques were applied on two laboratory small-scale wall samples before and after the application of a shear-compression diagonal load. Laboratory samples ($1 \times 1 \times 0.25$ m) are made of bricks and tuff respectively and reinforced with a thin high-strength and high-conductive fibre fabric. In order to improve the sample-antenna coupling in presence of conductive reinforcements, a Plexiglas plate was added underneath the 2 GHz antenna. GPR data were acquired along profiles spaced 0.1 m apart and ERT measurements were executed on a 0.1 m regular spaced grid with a dipole-dipole array operating in a three-dimensional configuration. GPR datasets were also analysed in non-conventional mode, by means of the picking of the reflection time of the EM wave from the rear face of the samples.

Results show that GPR and electrical resistivity tomography were both able to detect fractures and weakness zones caused by the load application, even though with a higher resolution for the georadar with respect to the geoelectrical method. The use of a dielectric material between the GPR antenna and the investigated medium improves substantially the signal penetration in the case of shallow high-conductive layers. Finally, three-dimensional synthetic simulations on the same samples validate the experimental evidences. Therefore, we demonstrate that this approach can be a reliable tool to monitor static load tests and it can be extended to the whole load cycle (before, during and after the experiment).

1. Introduction

The application of geophysical non-destructive testing can be an important tool for assessing the current state of a masonry structure. In light of this, geophysical methods were applied during last decades in order to detect and characterize structures without any damage [18]. In particular, ground penetrating radar (GPR) has been employed worldwide for evaluating the layer thicknesses [2]. It was also used for mapping of changes in materials or degraded zones [9,24], evaluation of water content [6,10,22] or clay content [7], and for location of reinforcing bars and metal elements in concrete bases or structures [5,31,39]. It was applied for characterization of different constructive materials [34], detection of cracks

* Corresponding author.
E-mail address: giorgio.dedonno@uniroma1.it (G. De Donno).

http://dx.doi.org/10.1016/j.conbuildmat.2017.06.112
0950-0618/

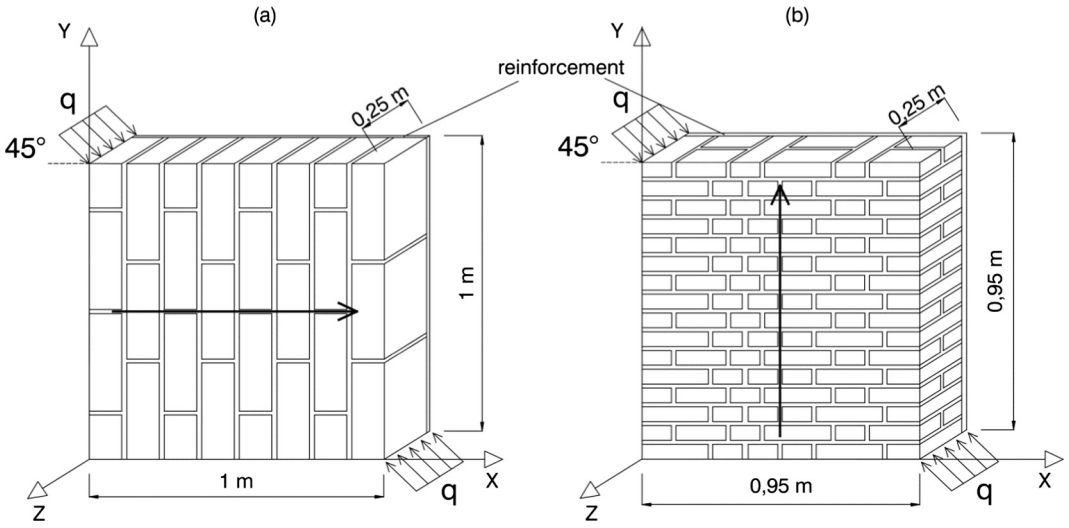

Fig. 1. Tuff (a) and bricks (b) laboratory samples. The applied load is marked with "q". Black arrows indicate the GPR profiles analysed in the text.

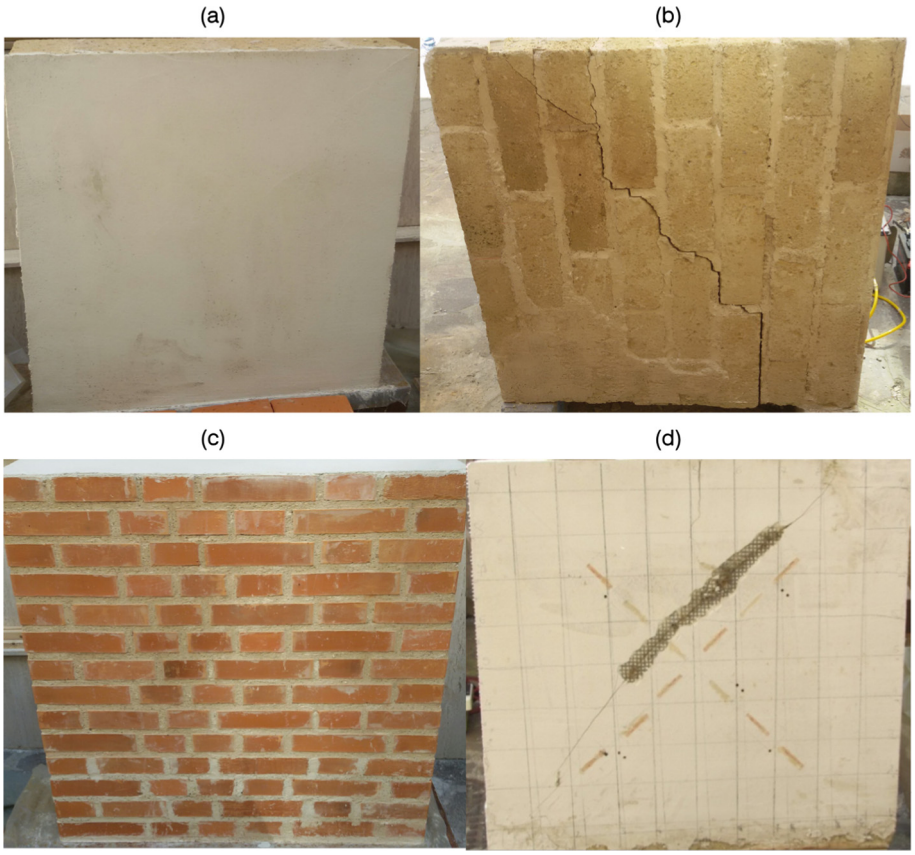

Fig. 2. Load test monitoring. Tuff sample before (a, reinforced face) and after (b, unreinforced face) the load application. Bricks sample before (c, unreinforced face) and after (d, reinforced face) the load application.

and fractures [3,29,28] and inspection of cultural heritage [14,20]. Through this method, a detailed image of the existent structures or important information about the location of buried elements (cavities, voids, fractures, reinforcements etc.) can be retrieved [21,12]. A review of GPR application for civil engineering can be found in Benedetto and Pajewski [8].

Although being a high-resolution technique, the GPR signal has the disadvantage of a lower depth of penetration in cases of conductive media [13], a case that often occurs for structural applications due to the presence of moisture, bricks or metallic objects (e.g. reinforcements). Furthermore, in many practical cases it is difficult to identify, with a sufficient degree of accuracy, the effective presence of fractures (mainly directed normally to the investigated surface), because the trace interval is often too large compared to the limited thickness of the fracture. In addition to this, it is not always feasible to establish a quantitative relationship between the GPR anomalies and the type of construction materials or of fractures, particularly for structures

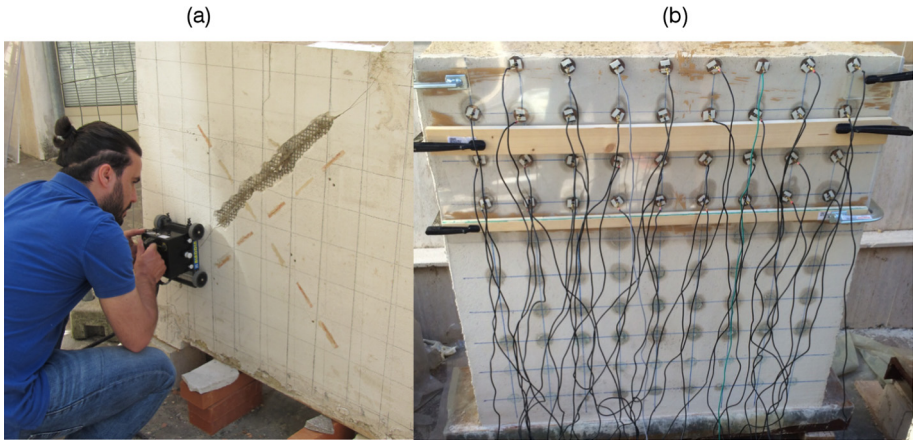

Fig. 3. Geophysical measurements on the masonry samples. (a) GPR investigation with a 2 GHz antenna and (b) 3D ERT investigation using 36 non-invasive cylindrical copper plates as electrodes.

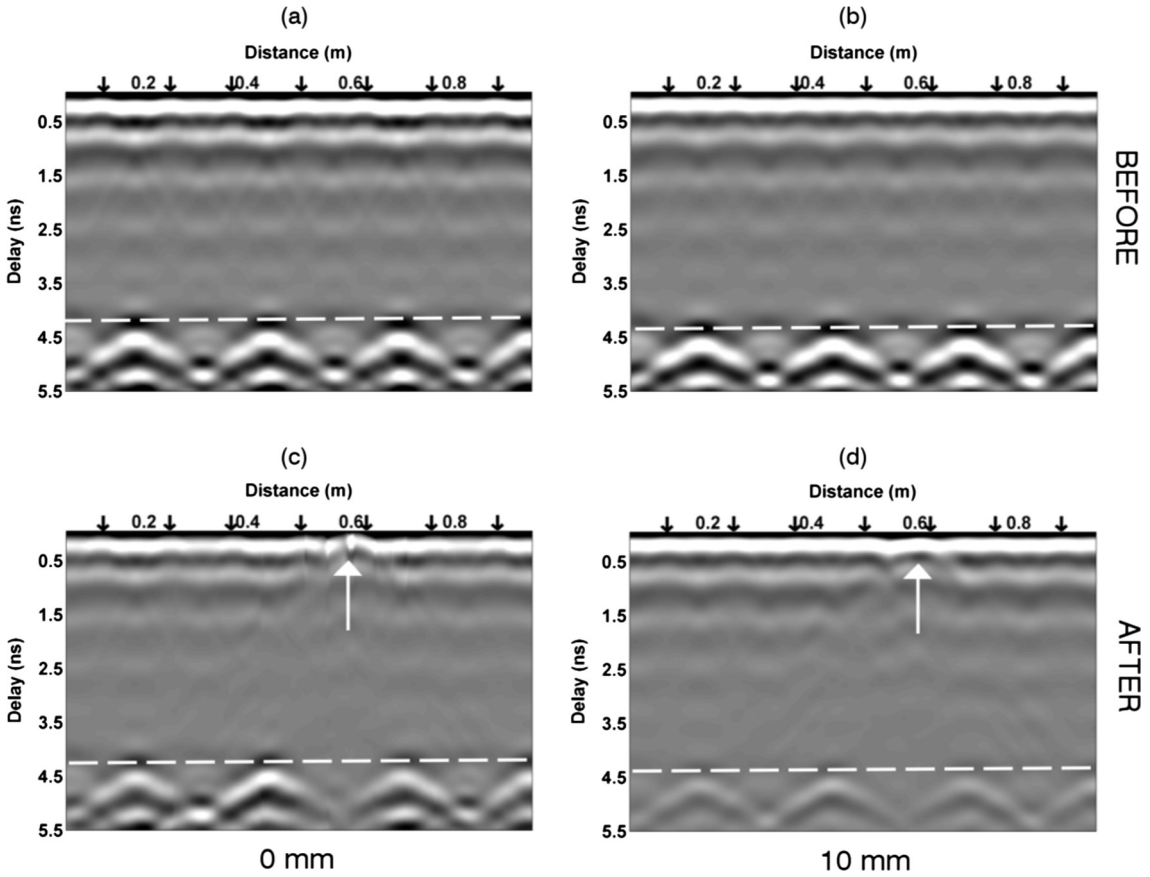

Fig. 4. Synthetic model of the laboratory tuff sample. Example GPR x-directed profile simulated at y = 0.5 m on the unreinforced face, before the load application without (a) and with 10 mm of Plexiglas (b) and after the load application without (c) and with 10 mm of Plexiglas (d). The white dashed line indicates the rear face of the sample, the white arrow the fracture location and the black arrows the location of mortar joints. Signal amplitude is normalised.

built with small-sized and heterogeneous materials combined together. In light of this, the integration of different geophysical techniques can help to reduce the degree of uncertainty. Electrical resistivity tomography (ERT) can be complementary employed for understanding the resistive behaviour of the construction materials, individuating defects or fractures, if any, and validating the GPR evidences. Given the electrical conductivity of the structure from ERT, we can also reduce the uncertainty in interpreting the low signal-to-noise ratio of the GPR data, which can be due to high degree of heterogeneities of materials or to an increase of conductivity. However, it is often difficult to ensure a correct coupling between electrodes and the investigated surface, using completely non-invasive electrodes, that is mandatory for investigating archaeological and structural targets without any damage. Moreover, the main disadvantage of ERT technique is the rapid loss of resolution in depth, which makes the detection of a small deep target impracticable. Therefore, ERT is rarely employed for structural monitoring, even though the use of ERT for archaeological application on masonries is not infrequent [27,32,37,11].

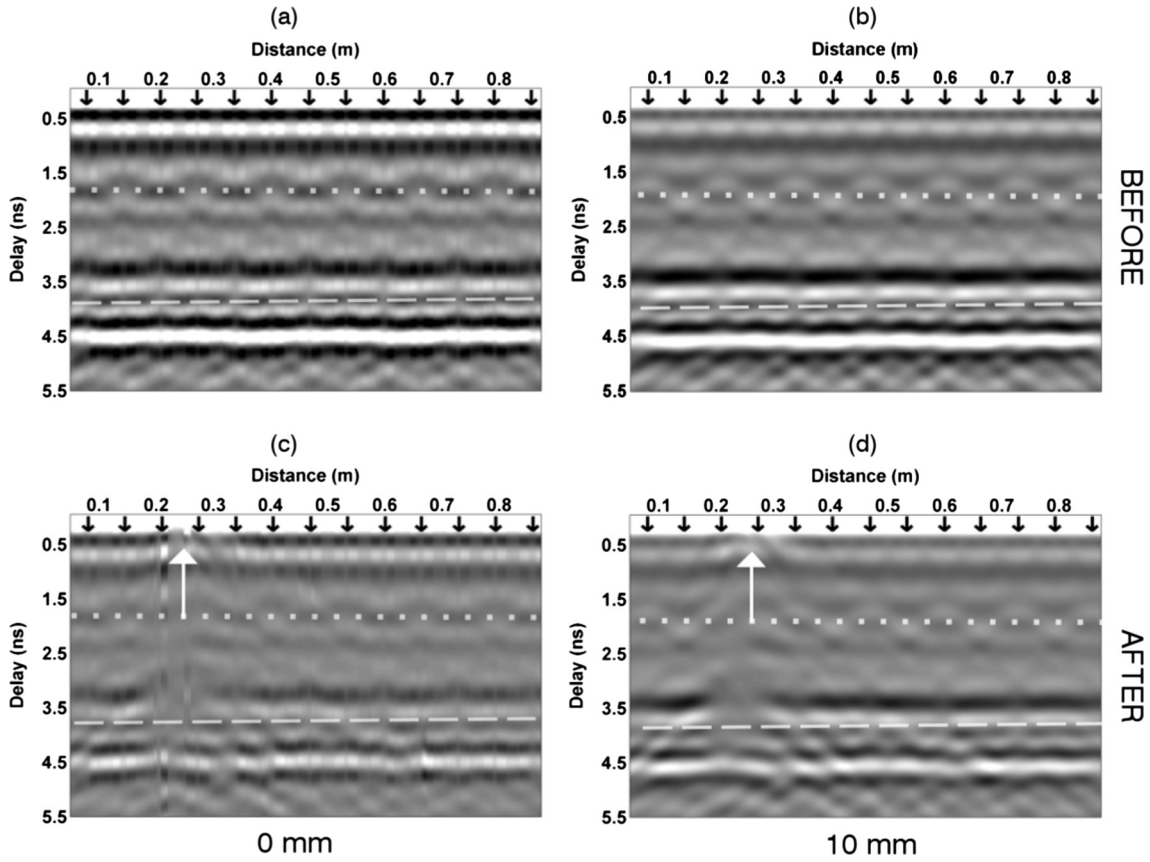

Fig. 5. Synthetic model of the laboratory bricks sample. Example GPR y-directed profile simulated at x = 0.5 m on the unreinforced face, before the load application without (a) and with 10 mm of Plexiglas (b) and after the load application without (c) and with 10 mm of Plexiglas (d). The white dashed line indicates the rear face of the sample, the white dotted line the end of the first row of bricks, the white arrow the fracture location and the black arrows the location of mortar joints. Signal amplitude is normalised.

Furthermore, the investigation of existing masonry buildings, widespread the historic centres, is requested because of their high seismic vulnerability highlighted by the recent earthquakes occurred in Central Italy (Summer and Autumn 2016), in order to understand potential and limits of reinforcements applicable to these structures. In this sense, laboratory load tests can help to evaluate benefit and drawbacks of materials in controlled conditions, for planning a future usage as reinforcement of masonry buildings. During last decades, examples of load test monitoring made by the analysis of electrical resistivity can be found in literature [33], even though the fracturing patterns occurring within the masonry can remain unknown. A step forward in this sense could be represented by the application of non-invasive methods in order to retrieve 2D or 3D maps of the studied parameters directly linkable with the cracks propagation.

Given the above mentioned open problems, the aim of this work is to understand potential and limits of GPR investigation of masonry, starting from the controlled laboratory conditions, where tuff and bricks small-scale samples were built up and subjected to a shear-compressional load. These materials had been commonly employed in Italy for decades for the construction of masonry building and consequently a large part of the historic centres, prone to earthquakes, was built using tuff blocks or bricks. We also aim to explore the change in the GPR response due to the different construction materials (tuff, bricks and reinforcements) and the benefit given by a dielectric layer, placed underneath the GPR antenna, for detecting the different anomalies.

In the following sections, we will describe the masonry samples together with the acquisition parameters and the processing procedures (Section 2), while results from both synthetic simulation and field acquisition are presented in Section 3, also analysing the benefit of the integration between GPR and ERT dataset for improving the interpretation of geophysical models.

2. Materials and methods

2.1. Sample geometry and materials

In this study we present the experiment on two masonry samples (Fig. 1), built with tuff blocks (330 × 110 × 240 mm) and bricks (225 × 50 × 100 mm). Overall, the tuff sample is 1 m long, 1 m high and 0.25 m wide (Fig. 1a), while the bricks sample is 0.95 × 0.95 × 0.25 m (Fig. 1b), both fibre-reinforced only on one face with a thin (2 mm), high-strength basalt fibre fabric mixed with stainless steel microwires [25] and embedded within a 10 mm thick mortar layer (Fig. 1). The reinforcement has a mixed resistive (basalt fibre) and conductive (steel wires) behaviour, even though overall it can be considered as a high-conductive material, as confirmed by 1D laboratory test, which we performed on small samples. Unlike the tuff (Fig. 1a), bricks are disposed into one or two rows, as shown in Fig. 1b.

The static load tests were executed on both samples through the application of a combined diagonal compression-shear load, that is a nominal capacity of $q = 250$ kN applied in compression with an angle of 45° referred to the x-axis (Fig. 1), following the ASTM-E519 standard [4] for diagonal load testing [25].

Geophysical measurements (GPR and ERT) were acquired before and after the load application (under load was technically unfeasible, due to safety reasons), on both samples. In Fig. 2 we report the images of the tuff and bricks samples before (Fig. 2a,c) and after the load application (Fig. 2b,d), respectively.

The mapping of the construction materials and of the fractures was executed by the visual inspection of the sample, before and after the load test.

2.2. Data acquisition and processing

2.2.1. Ground penetrating radar

GPR survey was performed on both main faces (reinforced and not) on a regular grid, spaced 0.1 m apart in both x- and y-directions (Fig. 3a). The data were collected using an IDS instrument equipped with a 2 GHz antenna and set with a trace

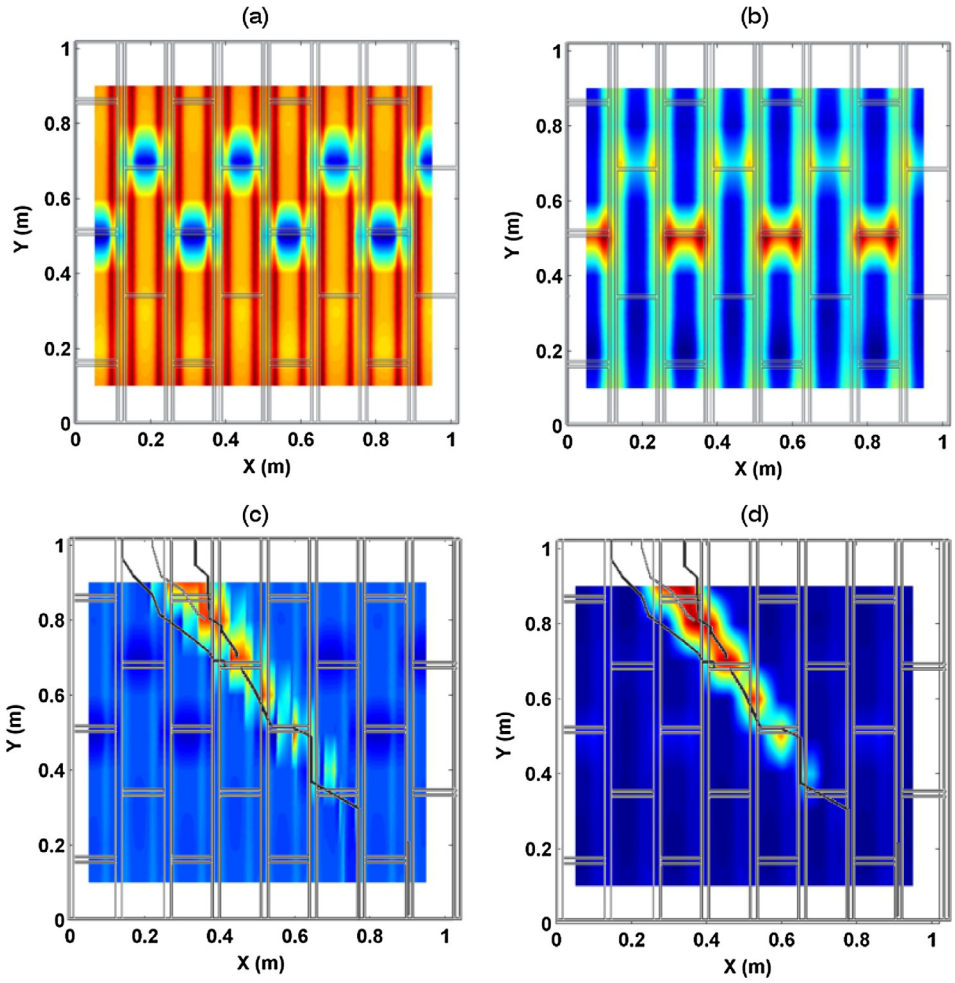

Fig. 6. Synthetic model of the laboratory tuff sample. GPR time-slice before the load application without (a) and with 10 mm of Plexiglas (b), and after the load application without (c) and with 10 mm of Plexiglas (d). Time slices are drawn at a depth of 50 ± 50 mm, considering both x- and y-directed profiles (colour scale in normalised units).

increment of 3 mm, a sample rate of 0.03 ns with a time window of 15 ns and an offset from the external boundary of 8 mm in the direction of acquisition and 10 mm in the normal direction. This configuration results in 9 GPR profiles for both directions. Although a denser sampling of GPR profiles is theoretically possible, we prefer to adopt a cost-effective sampling, directly applicable for common field surveys, in order to strike a balance between resolution needed and costs.

Measurements were executed with the antenna directly on the wall surface (configuration no. 1) and interposing a Plexiglas plate (1 × 1 m) having different thicknesses: 2.5 (no. 2), 5 (no. 3) and 10 mm (no. 4), between the GPR antenna and the wall surface. Therefore, we collected four dataset for each face of the two samples (tuff and bricks), both before and after of the load application.

The recorded signals were analysed by means of three different steps. Firstly, we executed a conventional data interpretation. To this end, data were processed by moving the start time, applying a band-pass filter (100–3200 MHz), a linear gain for trace amplitude equalization, a background removal for suppressing coherent noise and recovering the energy losses with depth and a migration procedure using the Stolt algorithm [36]. Then, time-slices (horizontal sections of the reflected and diffracted energy at different times) were extracted from the three-dimensional cube of GPR data, by averaging squared amplitude of GPR signal within a fixed depth window (100 mm) and interpolating data related both to x- and y-directed profiles [19]. For the time to depth conversion we used a constant velocity of 12 cm/ns for the bricks sample and 11 cm/ns for the tuff sample, obtained as the mean velocity of the fitting hyperbola related to the diffraction produced by the edge of the blocks and from the picking of the EM wave travel time to and from the rear face of the sample.

In addition to this standard processing, we aimed to have an estimation of the dielectric constant (or relative electrical permittivity, ε_r) variation within the samples, as an effect of the load test. In fact, a decrease of the dielectric constant can be related for unsaturated media to an increase of air-filled weakness zones or fractures. This relation can be achieved taking into account the travel time to and from the rear face of the sample (t_p), before and after the load application, knowing the thickness of the sample. In fact, under the hypothesis of dielectric media, that holds for $\left(\frac{\sigma^2}{\omega\varepsilon}\right)^2 \ll 1$, we have:

$$\varepsilon_r = \left(\frac{c \cdot t_p}{2s}\right)^2, \tag{1}$$

where c is the speed of light and s the thickness of the sample (0.25 m in this case). The above mentioned hypothesis holds for resistivity values >100 Ωm. Laboratory 1D electrical measurements (single quadrupole) performed on single tuff blocks and bricks give a resistivity value around 500 and 300 Ωm, respectively. The picking of the travel time t_p was executed for each trace position (i, j) where $i = 1, 2, \ldots, N$ and $j = 1, 2, \ldots, M$, being N the number of traces and M the number of profiles. Once t_p and s are known, we calculated the dielectric constant through Eq. (1) and consequently its variation within the samples, both before and after the load application. Any changes of the dielectric constant can be due to different type or arrangement of the building materials and to the presence of cracks and voids.

Finally, the variation of signal attenuation as a function of the quality (composition, degree of fracturing, etc.) of the sample was mapped. Practically we introduced the mean absolute amplitude (MAA) of the recorded signal, calculated within a time window extended up to t_p. Therefore, we have for each point (i,j):

$$MAA^{(i,j)} = \frac{1}{L^{(i,j)}} \sum_{k=1}^{L^{(i,j)}} \left| A_k^{(i,j)} \right|, \tag{2}$$

where A is the signal amplitude and L the number of time samples for trace i at the profile j. Both calculations (dielectric constant and MAA) were performed on raw data.

2.2.2. Electrical resistivity tomography

The geo-electrical dataset was acquired using 36 non-invasive cylindrical copper plates as electrodes (diameter = 30 mm, thickness = 3 mm), fixed on the wall through a 1 × 1 m Plexiglas plate, while clamps and a conductive gel contribute to improve the electrodes-sample coupling (Fig. 3b). Thus, we achieved a good coupling without any damage of the samples. The 48 electrodes were organized into 4 rows of 9 electrodes each, and they were progressively moved from the bottom to the top of the sample, overlapping two rows for each position shift, in order to

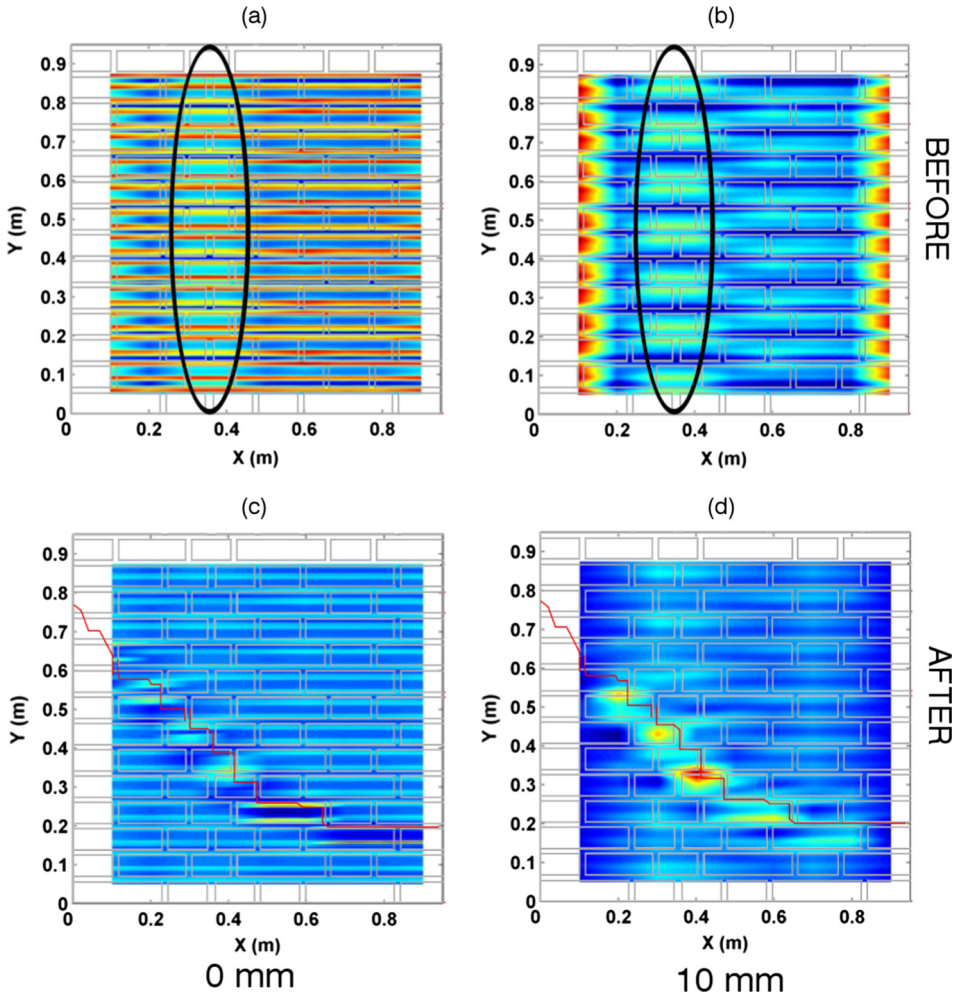

Fig. 7. Synthetic model of the laboratory bricks sample. GPR time-slice before the load application without (a) and with 10 mm of Plexiglas (b), and after the load application without (c) and with 10 mm of Plexiglas (d). Time slices are drawn at a depth of 50 ± 50 mm, considering both x- and y-directed profiles (colour scale in normalised units). The black ellipses indicate the location of the single row of bricks.

obtain a homogeneous data coverage. Data were acquired using the IRIS Syscal Pro 48 resistivimeter with a three-dimensional dipole-dipole "snake" array for each position, leading to 3426 apparent resistivity measurements for each configuration (tuff and bricks, before and after the load test). The survey on the fibre-reinforced face was unfeasible due to the high-conductivity of the reinforcement that prevented the investigation of the deeper layers.

Apparent resistivity data were inverted using the VEMI algorithm [17], a Matlab-based open-source algorithm included in EIDORS [1], able to invert 3D electrical data, using a finite element approach with tetrahedral elements for solving the forward problem [16] and a Gauss-Newton procedure with optimized damping for inversion [15]. A Neumann-type boundary condition was imposed on all the faces of the samples, in order to simulate the absence of current flow through the air-sample interface, differently from a standard geo-electrical processing.

3. Results

Firstly, we discuss below the GPR synthetic modelling (Section 3.1) and in a following section (3.2) the results of GPR and ERT laboratory data.

3.1. GPR synthetic modelling

Since we know geometry and materials of the investigated medium, we firstly performed synthetic simulations on the models shown in Fig. 1, using the same acquisition parameters of the laboratory data. Simulations were carried out through gprMax v.3 [38], using a value of the dielectric constant equal to 6 for tuff blocks, 7 for bricks and 4.5 for mortar [26,30]. The complex fracturing patterns detected after the load application (Fig. 2b,d) was simulated by adding a series of prismatic thin zones (thickness = 4 mm) in which the free space condition ($\varepsilon_r = 1$) was imposed. In all scans, the GPR antenna was modelled using a 1.5 GHz ricker pulse, with a spatial discretization of 3.5 mm in all directions and a time window of 7 ns. The synthetic dataset was processed with the same procedures described above for the standard processing of laboratory data. The main goal of the synthetic simulation was to assess the possible benefit of the Plexiglas interposition and to validate the interpretation of the laboratory data, evaluating also the capability of the GPR system to detect fractures for these construction materials. The simulation of the GPR survey on the reinforced face was not practical, due to the high complexity of the reinforcement, where a high-conductive material (steel wires) is combined together with a dielectric material (basalt fibre). Therefore, we present results from synthetic simulations on the unreinforced face of the two samples.

Results of simulations are shown in Figs. 4 and 5 in terms of GPR sections for both samples before and after the load application, located as shown in Fig. 1, while in Figs. 6 and 7 the respective time-slices drawn at a depth of 50 mm considering a window of 0–100 mm for the same configurations are shown.

The tuff radargrams (Fig. 4) show that the added value of the Plexiglas interposition is negligible for simulations performed on the unreinforced face. However, we have a loss of resolution using Plexiglas, as expected, that prevents the detection of the mortar

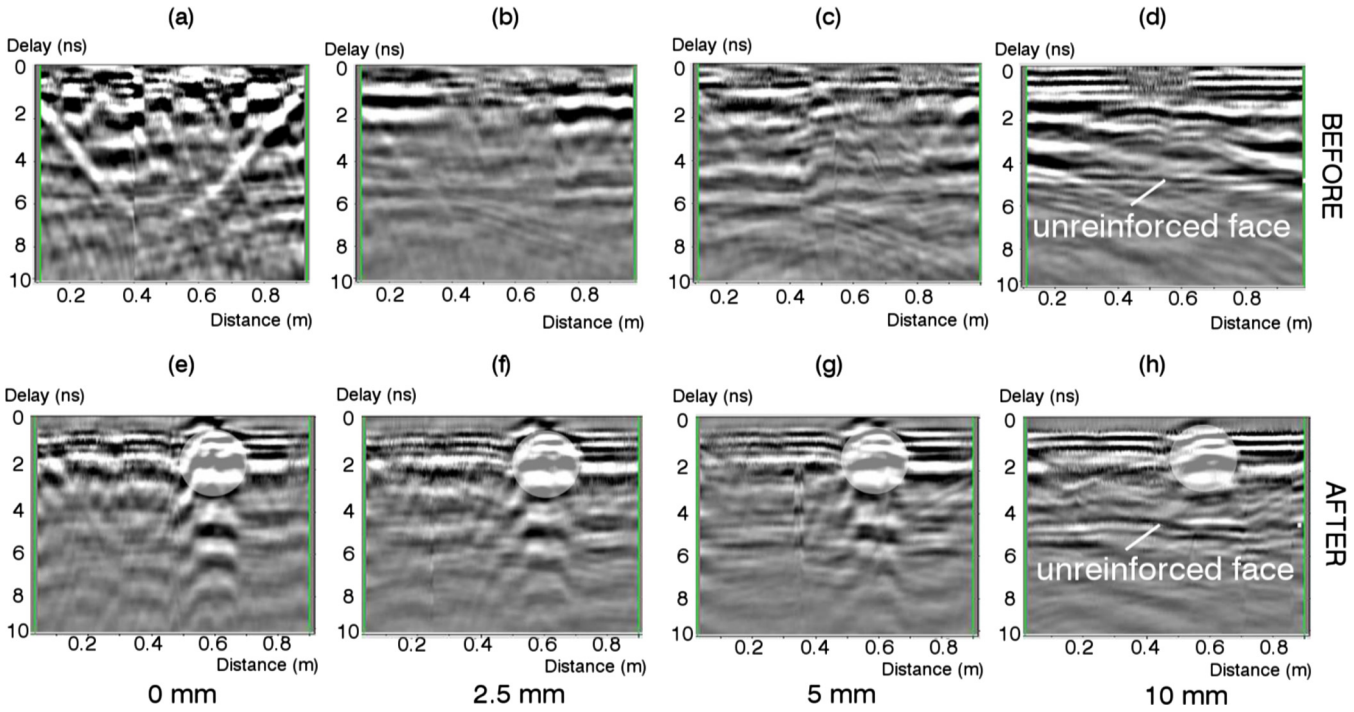

Fig. 8. Laboratory tuff sample. Example GPR x-directed profile acquired at y = 0.5 m on the fibre-reinforced face, before the load application without (a) and with 2.5 (b), 5 (c) and 10 mm of Plexiglas (d) and after the load application without (e) and with 2.5 (f), 5 (g) and 10 mm of Plexiglas (h). The white circles indicate the zones where the steel-basalt fibre fabric is coupled with the GPR antenna.

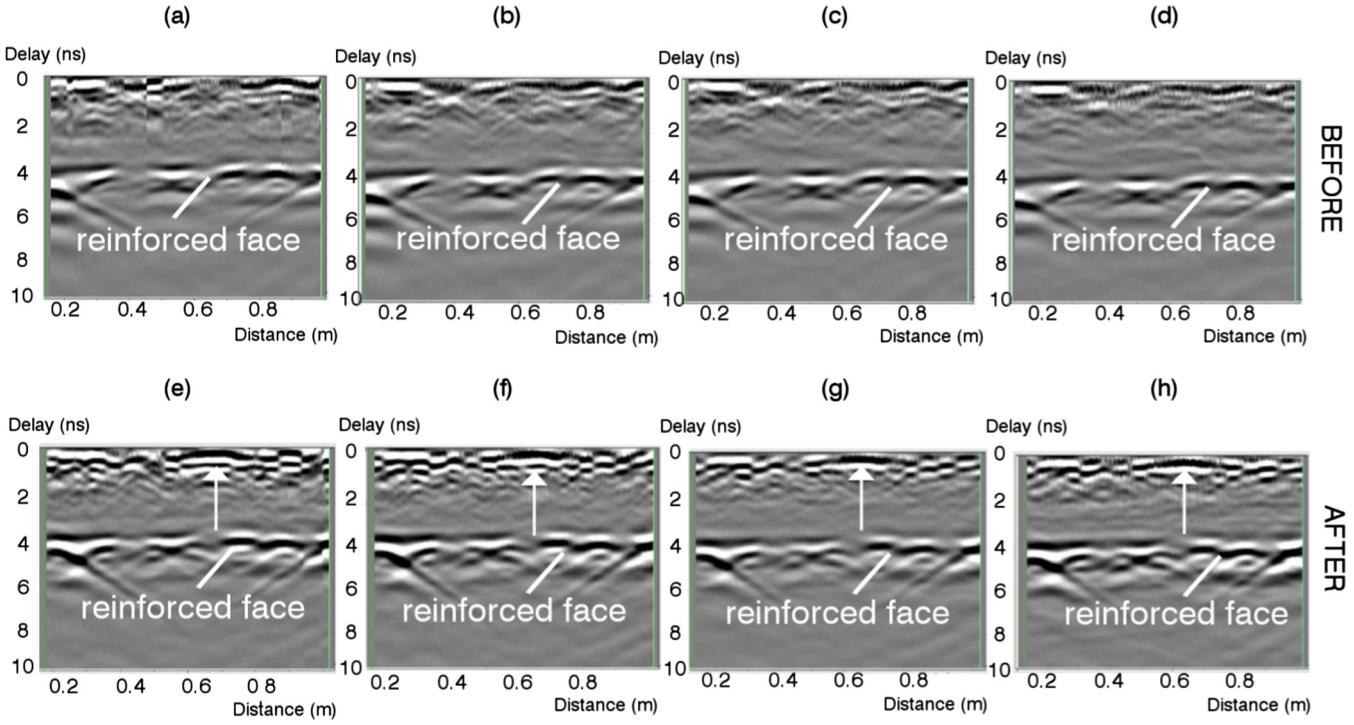

Fig. 9. Laboratory tuff sample. Example GPR x-directed profile acquired at y = 0.5 m on the unreinforced face, before the load application without (a) and with 2.5 (b), 5 (c) and 10 mm of Plexiglas (d) and after the load application without (e) and with 2.5 (f), 5 (g) and 10 mm of Plexiglas (h). The white arrows indicate the fracture location.

joints between the blocks (black arrows), while the rear face of the sample (dashed line) and the fracture are well detected (white arrow) by both configurations.

Similar results were obtained for the bricks sample (Fig. 5), where joints (blacks arrows) remains almost undistinguishable using Plexiglas, while the discontinuity between the two rows of bricks (dotted line) is clearly visible in all GPR sections.

The time-slices confirm the evidences early revealed by GPR profiles for both samples.

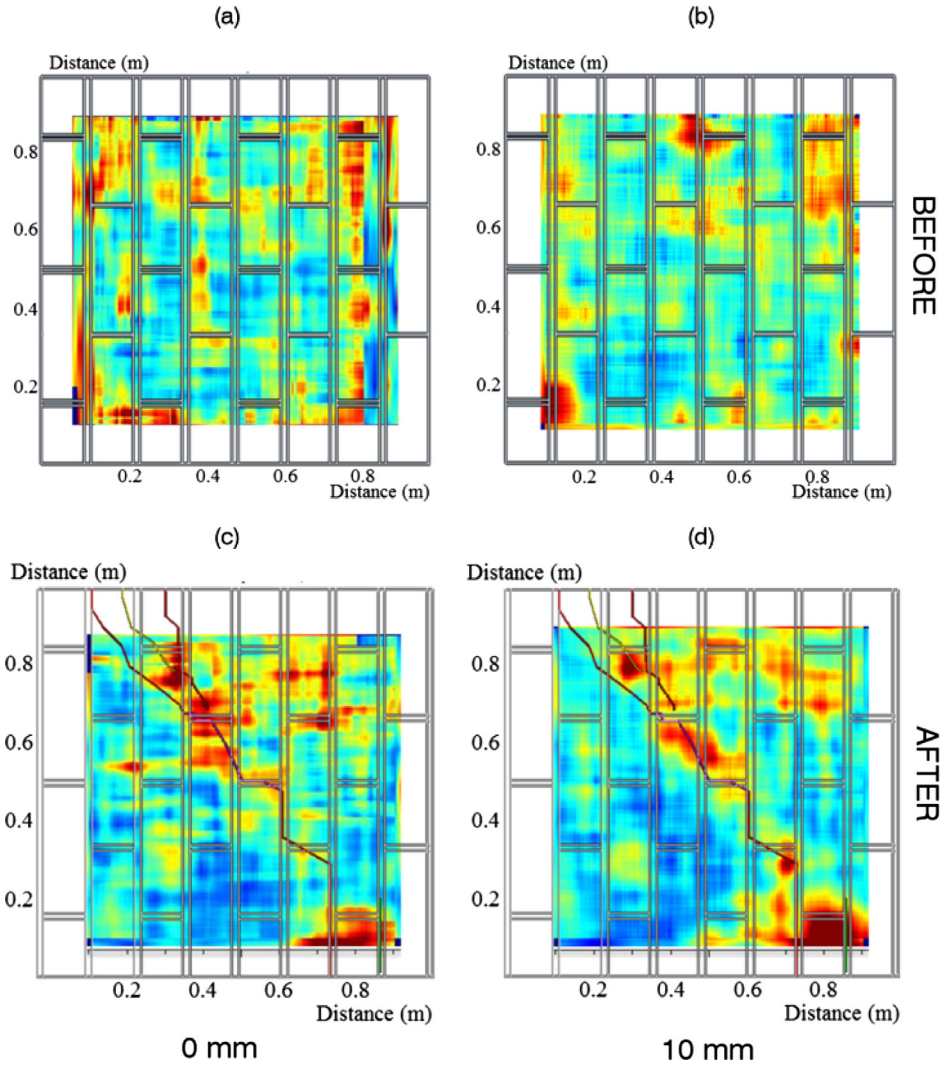

Fig. 10. Laboratory tuff sample. GPR time-slice before the load application without (a) and with 10 mm of Plexiglas (b), and after the load application without (c) and with 10 mm of Plexiglas (d). Time slices are drawn at a depth of 50 ± 50 mm, considering both x- and y-directed profiles (colour scale in normalised units).

In fact we have for the tuff sample a higher resolution in the model where Plexiglas (Fig. 6a,c) was not used; otherwise (Fig. 6b,d) the joints remains visible, even though with less amplitude compared to that of the fracture (Fig. 6d). The amplitude of the GPR signal seen on the undisturbed configuration (Fig. 6a,b) strongly depends on the direction and the location of the profile compared with the object to be detected: in fact x-directed joints are detected only where they are exactly superimposed with the GPR profile (e.g. y = 0.5 m and 0.7 m).

For the bricks sample (Fig. 7), in which the small-sized objects are included, the effect of the location of the GPR profile with respect to the joint position is enhanced on the time-slices. In addition, a different response can be seen in the zone where the bricks are elongated in the z-direction only one row of bricks, black ellipses) with higher reflectivity with respect to the zone where they are combined both in the x- and in the z-directions. In both cases, Plexiglas improves the capability of detecting the fracture. This improvement may involve the coupling effect and consequently the spectrum of the radar pulse. In fact, according to Liu et al. [23], the spectrum centroid of a radar pulse experiences a downshift during propagation as a result of linear frequency dependence of attenuation. The centroid downshift is proportional to the integral of an intrinsic attenuation coefficient with respect to length along the ray-path. By assuming that the process of wave propagation can be described by linear system theory, if the amplitude spectrum of an incident wave is $S(f)$, and the medium and instrument response is $G(f)\cdot H(f)$, then the received amplitude spectrum $R(f)$, may be, in general, expressed as:

$$R(f) = G(f) \cdot H(f) \cdot S(f), \tag{3}$$

where the factor $G(f)$ includes geometric spreading, instrument response, source and receiver coupling to the medium, antenna radiation pattern, reflection and transmission coefficients, and the phase accumulation due to propagation, and $H(f)$ describes the attenuation effect on the amplitude. Frequency-dependent attenuation causes a change in the amplitude spectra. For a linear model and a Gaussian spectrum the difference in centroid frequency between the incident input and transmitted output waves is proportional to the integrated attenuation multiplied by a scaling factor [23]. The coupling effects of two electric dipoles on an interface was analysed by Slob and Fokkema [35]. They determined for the H-plane receiver, a drop of the peak amplitude by more than a factor of 2 when the antenna is on the surface of a $\varepsilon_r = 5$ half-space compared to an antenna in air, and by a factor of 4 when changing from $\varepsilon_r = 5$ to $\varepsilon_r = 10$. This is all due to interference differences. For $\varepsilon_r = 10$ the antenna separation is more than a dominant wavelength and

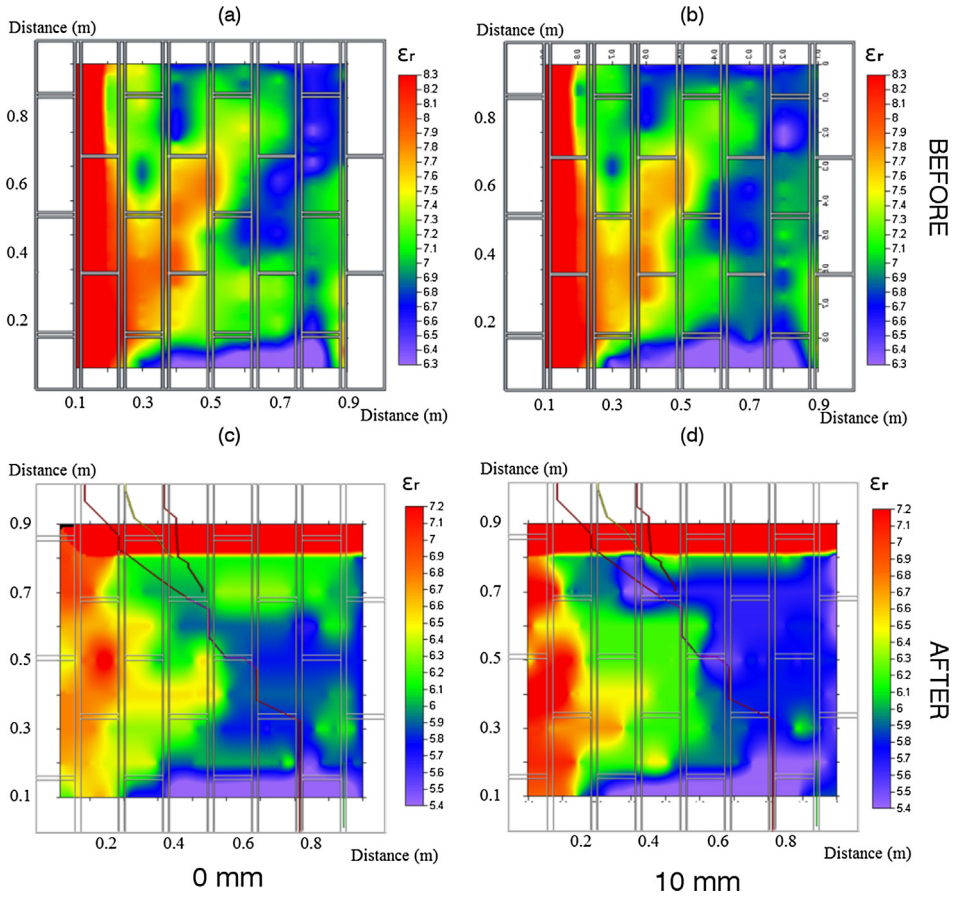

Fig. 11. Dielectric constant calculated for the laboratory tuff sample before the load application, without (a) and with 10 mm of Plexiglas (b), and after the load application without (c) and with 10 mm of Plexiglas (d).

increasing the permittivity further results in amplitude decrease that can be understood from the separate arrivals of the direct air and ground waves.

Therefore, the main benefit of the Plexiglas interposition is the reduction of the drop of the peak amplitude at the cost of a frequency downshift that can affect resolution.

Thus, results of synthetic examples highlight the pivotal role of the masonry composition and heterogeneity in the GPR response and the improvement on identification of fractures thanks to the Plexiglas layer.

3.2. Laboratory test

3.2.1. Tuff sample

At first, we explore thoroughly the benefit of the Plexiglas interposition between surface and antenna by the analysis of the GPR profiles acquired on the fibre-reinforced face of the tuff sample (Fig. 8). The radargrams are related to the GPR mid-profile (y = 0.5 m in Fig. 1) acquired with the four Plexiglas configurations, both before and after the load test.

Results demonstrate that the Plexiglas interposition can improve substantially the antenna coupling and consequently the capability to detect the fractures and the rear face of the sample (Fig. 8d and h), despite losing resolution. In fact, we are able to identify the rear face of the sample only using the 10 mm thick Plexiglas plate (Fig. 8d and h), otherwise the unreinforced face remains undistinguishable (Fig. 8a and e) even with thinner layers of Plexiglas (Fig. 8b, c, f and g). The reverberation shown after load (Fig. 8e-h at x = 0.6 m) is located in correspondence of the main fracture, where the mortar layer was removed in order to investigate directly the integrity of the fabric after the loading process. Consequently here the GPR antenna is directly coupled with the steel-basalt fabric.

The investigation of the samples on the unreinforced face is directly comparable with the synthetic examples of Figs. 4–7. Therefore, for these cases, we fully apply the processing procedure (radargrams, time-slices, maps of the dielectric constant and of the mean absolute amplitude). GPR x-directed profiles, acquired at y = 0.5 m, are represented in Fig. 9 and are comparable with the respective synthetic radargrams of Fig. 4.

The reinforced face is always well-detected (Fig. 9) without significant differences among the different thickness of Plexiglas, as expected after the simulations (Fig. 4). The joints between the blocks are not clearly detected, compared to the synthetic examples, due to the roughness of the surface and the heterogeneity of blocks. After the load test (Fig. 9e-h) the first part of the radargram (t = 0–2 ns) is more reflective due to the weakening of the mortar and to the presence of fractures. On the basis of the results shown by the GPR profiles, we decided to narrow the following analysis only considering the configuration no. 1 (without Plexiglas, Fig. 9a,e) and no. 4 (10 mm, Fig. 9d,h), for the sake of simplicity. The respective time-slices, drawn at a depth of 50 ± 50 mm, are depicted in Fig. 10.

The results confirm the main issue underlined by the numerical simulations (Fig. 6): where the antenna is placed directly on the sample surface (Fig. 10a) we have a higher resolution and a higher reflectivity at the joints although signal is more scattered, compared with the case where Plexiglas is used (Fig. 10b). After the

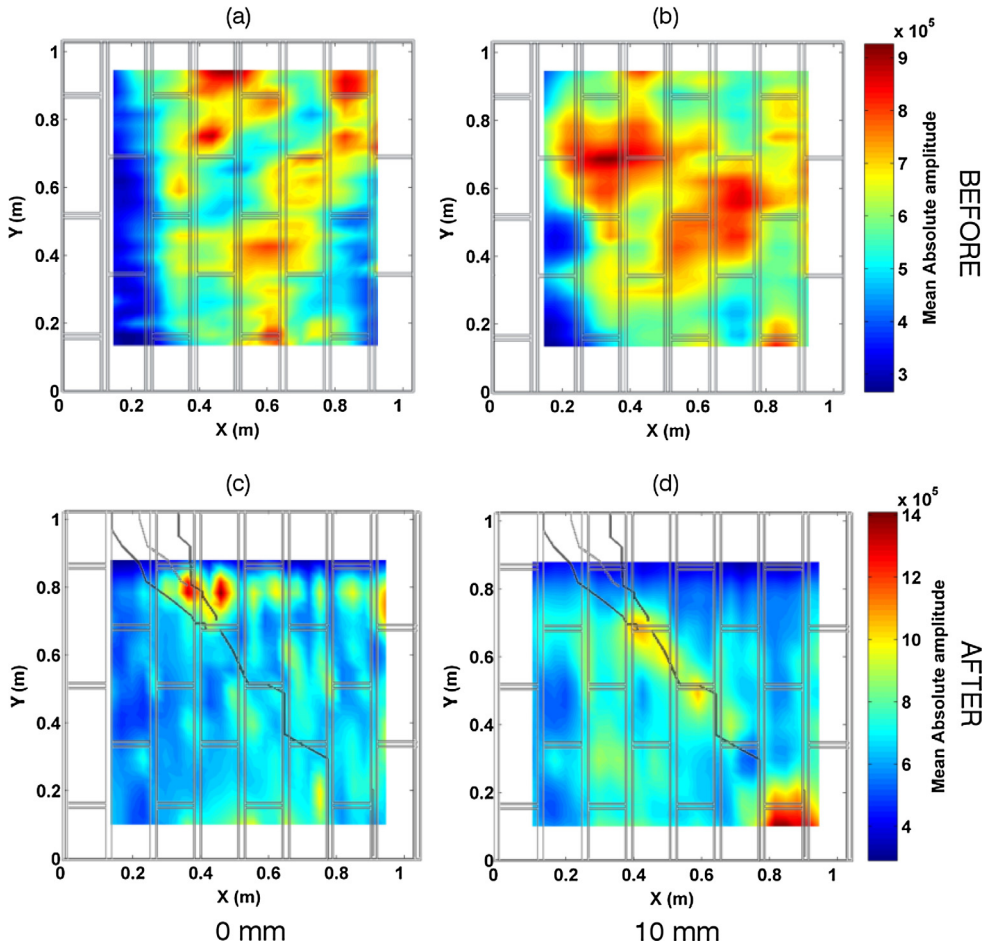

Fig. 12. Mean absolute amplitude calculated for the laboratory tuff sample before the load application, without (a) and with 10 mm of Plexiglas (b), and after the load application without (c) and with 10 mm of Plexiglas (d).

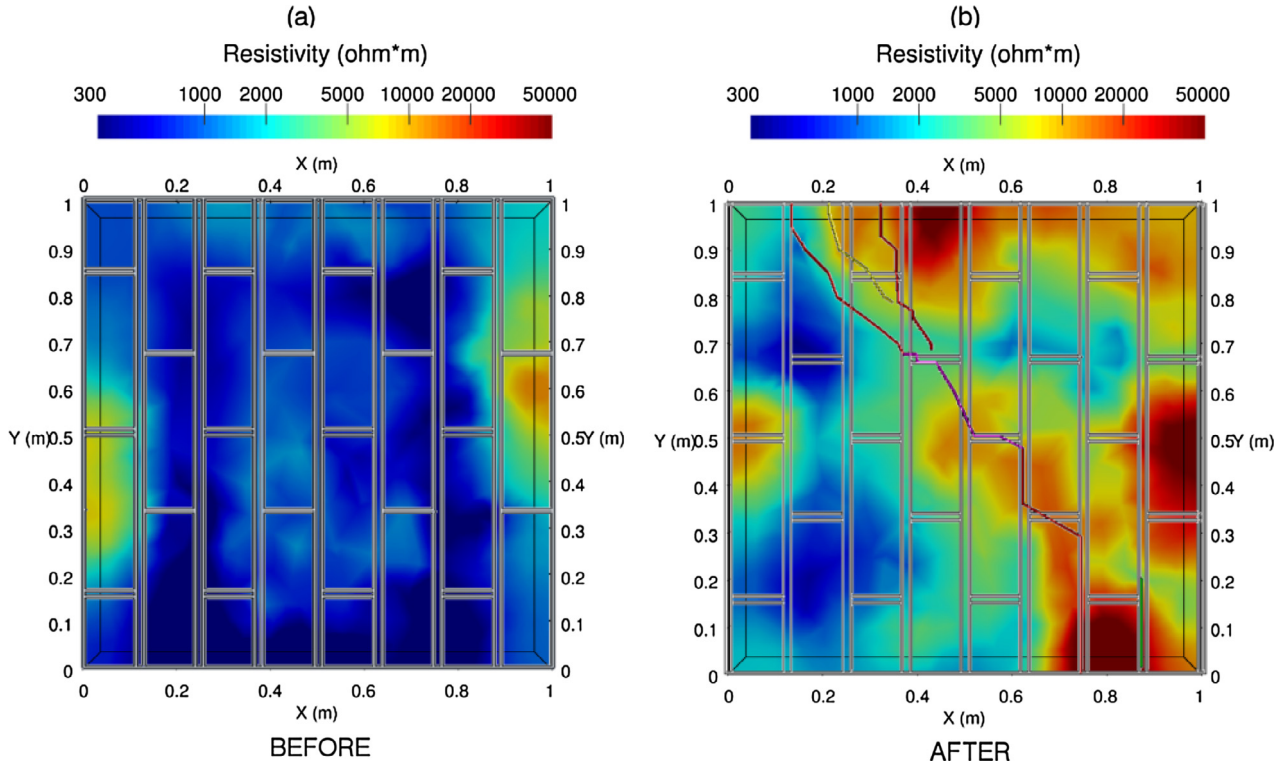

Fig. 13. 3D ERT inverted model for tuff sample before (a) and after (b) load application. Horizontal slices are drawn at a depth of 50 ± 50 mm.

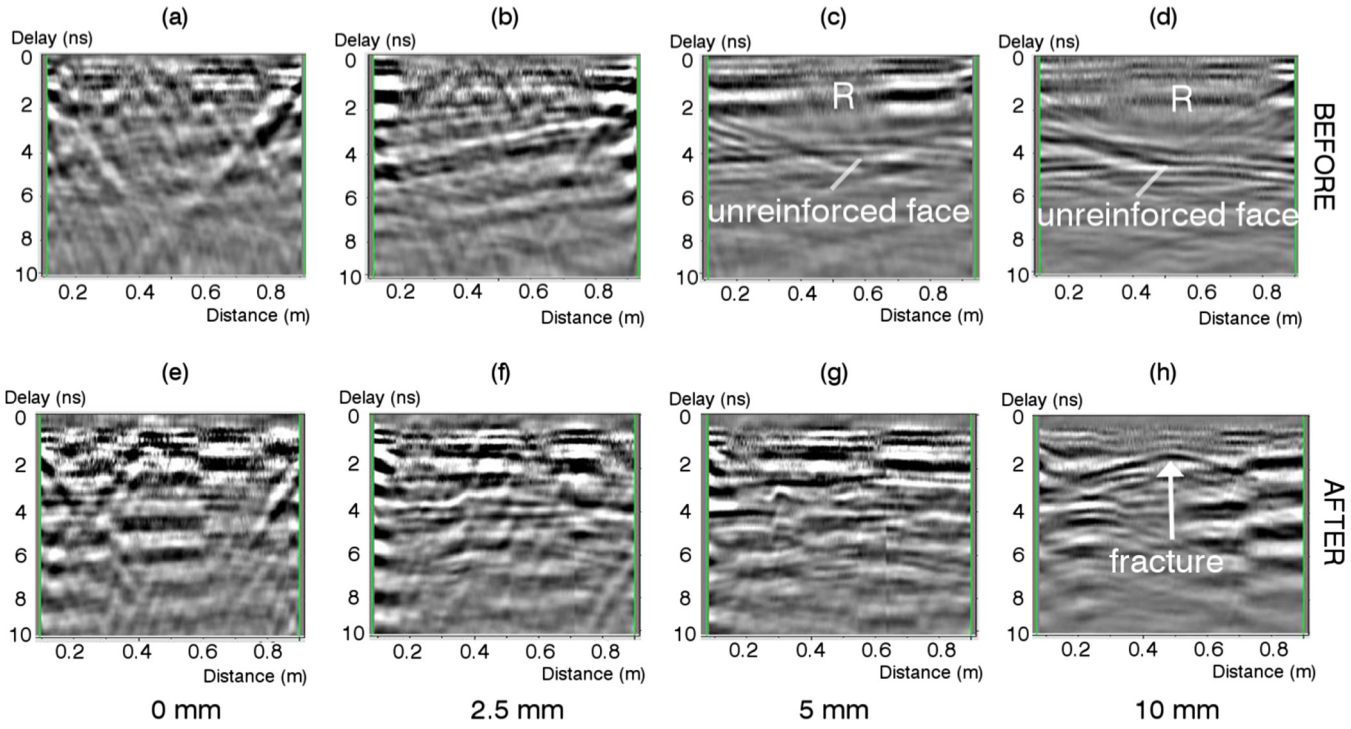

Fig. 14. Laboratory bricks sample. Example GPR y-directed profile acquired at x = 0.5 m on the fibre-reinforced face, before the load application without (a) and with 2.5 (b), 5 (c) and 10 mm of Plexiglas (d) and after the load application without (e) and with 2.5 (f), 5 (g) and 10 mm of Plexiglas (h). The letter "R" indicates the end of the first row of bricks.

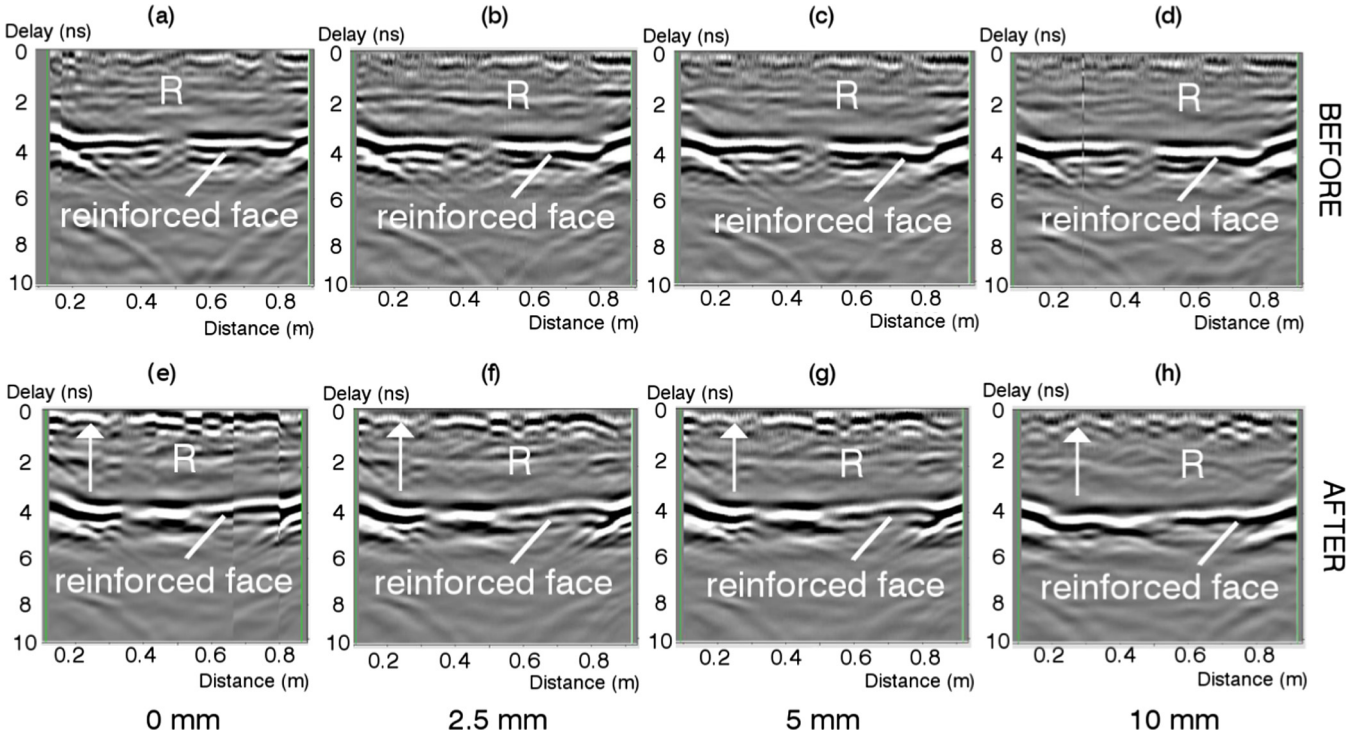

Fig. 15. Laboratory bricks sample. Example GPR y-directed profile acquired at x = 0.5 m on the unreinforced face, before the load application without (a) and with 2.5 (b), 5 (c) and 10 mm of Plexiglas (d) and after the load application without (e) and with 2.5 (f), 5 (g) and 10 mm of Plexiglas (h). The letter "R" indicates the end of the first row of bricks and the white arrows the fracture location.

application of the diagonal stress (Fig. 10c,d), both configurations are able to detect the main fractured zone and, as a consequence of the load application, the sample is divided into two main zones (above and below the main fracture), indicating how the stress has acted differently on the sample. The evidences of the time-slices are confirmed by the maps of the dielectric constant (Fig. 11), made

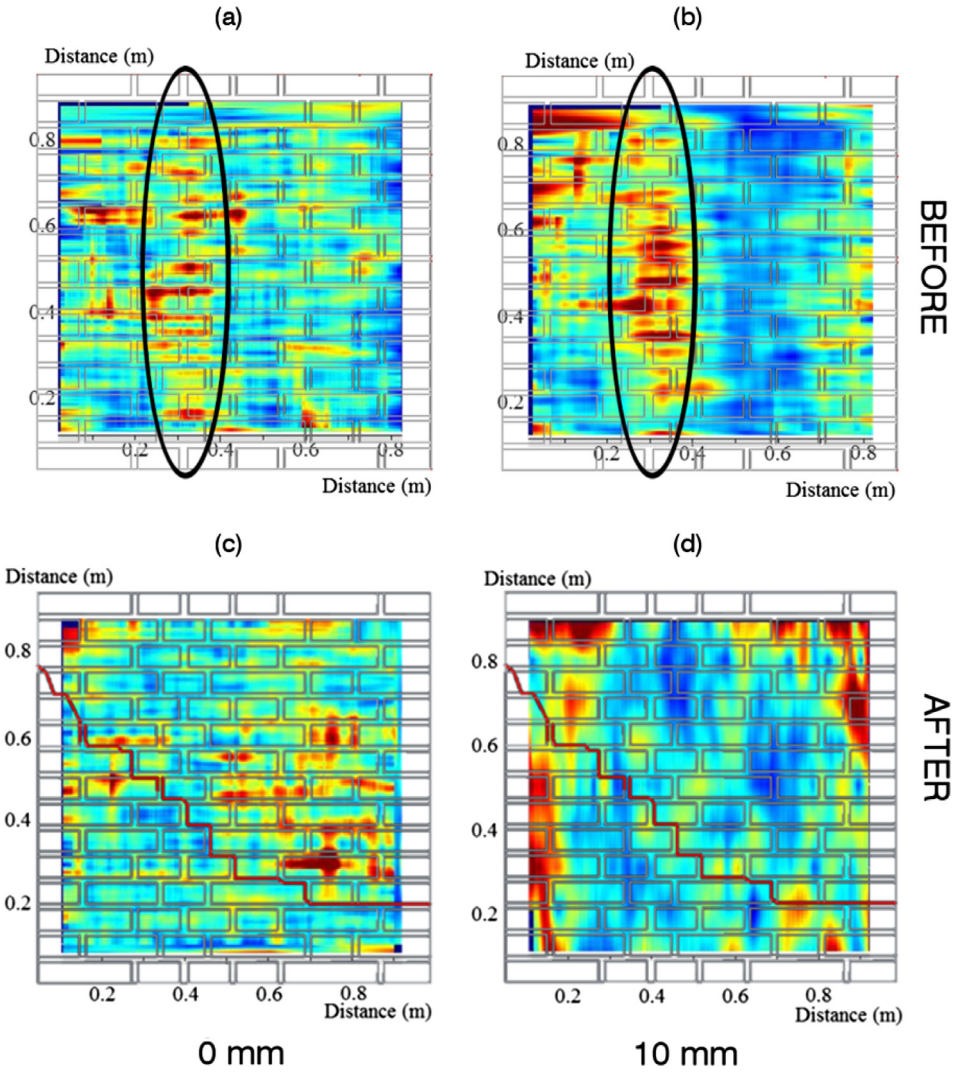

Fig. 16. Laboratory bricks sample. GPR time-slice before the load application without (a) and with 10 mm of Plexiglas (b). GPR time-slice after the load application without (c) and with 10 mm of Plexiglas (d). Time slices are drawn considering both x- and y-directed profiles (colour scale in normalised units). The black ellipses indicate the location of the single row of bricks. (For interpretation of the references to colour in this figure legend, the reader is referred to the web version of this article.)

using Eq. (1) starting from the picking of the EM wave travel time (t_p) on the deep reflector (rear face of the sample). In fact the GPR response, before load application, is mainly triggered by the samples geometry, while after the load test the sample has been rearranged as an effect of the stress undergone.

Before the load application (Fig. 11a,b), the tuff sample has a mean value of the dielectric constant around 7 (discarding the high values > 8, due to the effect of an adjacent steel beam located at x = 0.1–0.2 m). The effect of the steel beam is also visible on the x-directed radargrams of Fig. 9 as the diffraction hyperbola seen at x = 0.1–0.2 m. This effect causes an over-estimation of the EM wave travel-time and consequently of the dielectric constant (Eq. (1)).

After the load test (Fig. 11c,d), the mean value drops to 6 (discarding the high values > 7 located at y = 0.8–0.9 m, due to the effect of the adjacent steel beam, repositioned after the load test on the top of the sample) as a result of the intense fracturing occurred within the sample. Here, the sample is divided into two main zones, as seen before: above the main fracture, with relative lower values of ε_r (5.5–6.5) and below it, where the dielectric constant is slightly higher (6.5–7.5). Therefore, the high scattering, early highlighted in the upper-right zone by the time-slice in Fig. 10c,d, is mainly due to the noteworthy presence of micro-fractures in that weakness zone, with a consequent lowering of ε_r in Fig. 11c,d.

At the end, the MAA maps calculated with Eq. (2) for the undisturbed tuff sample (Fig. 12a,b), confirm the generally uniform response among the different configurations (with or without Plexiglas), observed before. After the load test the main fracture is clearly visible (in particular with the Plexiglas interposition, Fig. 12d). The low MAA values, visible at x = 0.1–0.2 m (before load test, Fig. 12a,b) y = 0.8–0.9 m (after load test, Fig. 12c,d) are due to the presence of the adjacent steel beam. Overall, we have higher MAA values after the load application (Fig. 12c,d) compared to those obtained before the load test (Fig. 12a,b).

Finally, GPR results are validated by the results of 3D ERT inversion, analysed in terms of the shallowest horizontal section (Fig. 13, depth = 50 ± 50 mm), directly comparable with the GPR time-slices of Fig. 10. In fact, since the resolution of the ERT method rapidly decrease with depth, the deeper sections have a degree of resolution not compatible with these goals. The undisturbed model (Fig. 13) is almost homogenous denoting a mean resistivity of 700 Ωm, comparable with the values obtained in the laboratory on single tuff blocks. After the load application,

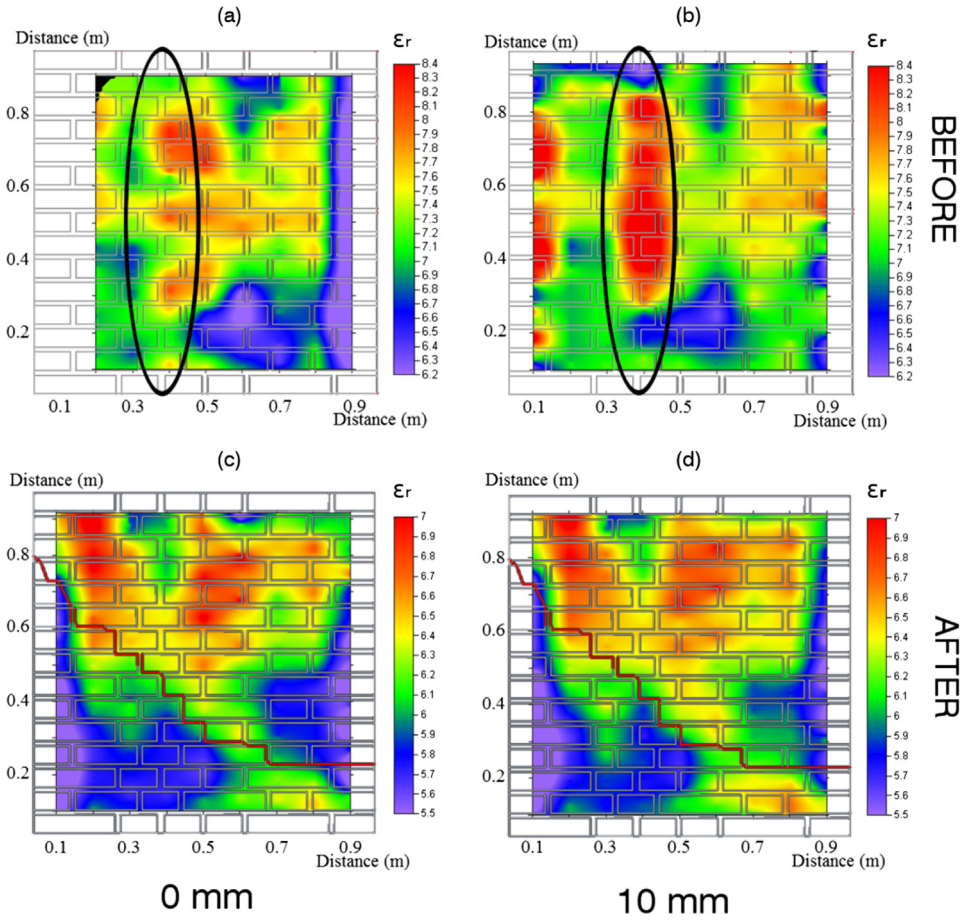

Fig. 17. Dielectric constant calculated for the laboratory bricks sample before the load application, without (a) and with 10 mm of Plexiglas (b), and after the load application without (c) and with 10 mm of Plexiglas (d). Maps are drawn considering both x- and y-directed profiles. The black ellipses indicate the location of the single row of bricks.

higher resistivity values (>1000 Ωm) are retrieved in correspondence of the fractures and of the weakness zones (top-right). These results confirm the GPR data results (decrease of dielectric constant and increase of reflectivity in the top-right part of sample), validating the hypothesis that this part of sample suffers more deformation then the other.

3.2.2. Bricks sample

Similarly to the tuff case, only using 5 and 10 mm thick Plexiglas plates, we are able to detect the rear face of the sample on the GPR profile acquired on the fibre-reinforced face (Fig. 14a,b,c, d). After the load application (Fig. 14e,f,g,h), the rear face of the sample is not visible at all, even using the dielectric layer. However, the 10 mm thick Plexiglas layer helps in detecting the fracture (Fig. 14h), that remains hidden on the other configurations (Fig. 14e, f and g).

The GPR profiles acquired on the unreinforced face (Fig. 15) help to identify the interface between two rows of bricks (letter "R") and the rear face of the sample with all the four configurations, accordingly to the respective synthetic radargrams (Fig. 5). The corresponding time-slices (Fig. 16) show that the response strongly depends on the samples geometry, confirming the evidences of the synthetic simulations (Fig. 7). In fact, where the z-directed bricks are juxtaposed, the signal is more scattered (black ellipse), as seen before for the respective synthetic example (Fig. 7a,b).

After the load test, the fracture mainly propagates within the joints, where we have high-scattering values (Fig. 16c,d), even though a clear correlation between the fracture and the GPR anomalies is not evident without Plexiglas (Fig. 16c) and barely visible using the 10 mm of Plexiglas (Fig. 16d). The high scattering seen in Fig. 16c (x = 0.6–0.8 m and y = 0.3–0.6 m) are maybe due local heterogeneities (micro-fractures within joints) of the bricks sample, enhanced with the absence of Plexiglas. The worse distinguishability of the main fracture, with respect to the tuff specimen, is therefore due to the higher heterogeneity of the bricks sample, both in terms of dimension and geometrical layout of the single component. In this sense the maps of dielectric constant should clarify the effective distribution of the fractured zones, being this index more sensible to the degree of fracturing of the whole sample. In fact, the undisturbed bricks sample (Fig. 17a,b) displays higher ε_r values (red zone) in correspondence of the single row of bricks (grey ellipse), while elsewhere ε_r is lower. Overall the mean dielectric constant is around 7.5, higher than the tuff as expected. The applied stress causes a rearrangement of the dielectric constant into two main zones (Fig. 17c,d): in the upper-right part we have higher $\boldsymbol{\varepsilon_r}$ values with respect to the bottom-left, where the fracturing is more intense. However, this effect is not seen in the respective time-slices of Fig. 16c,d. At the end the Plexiglas layer does not produce a remarkable effect on these maps.

The peculiar behaviour seen on the previous plots is confirmed in Fig. 18, where the MAA maps are represented. In fact, signal is strongly attenuated in presence of a single row of bricks (Fig. 18b), mainly due to the higher conductivity of the bricks with respect to the mortar and to the lower presence of reflections from the mortar joints, while higher values can be observed elsewhere.

As a result of the load test, the brick sample shows a higher signal amplitude in the bottom-left part of the sample (Fig. 18c,d), accordingly with the evidences of Fig. 17.

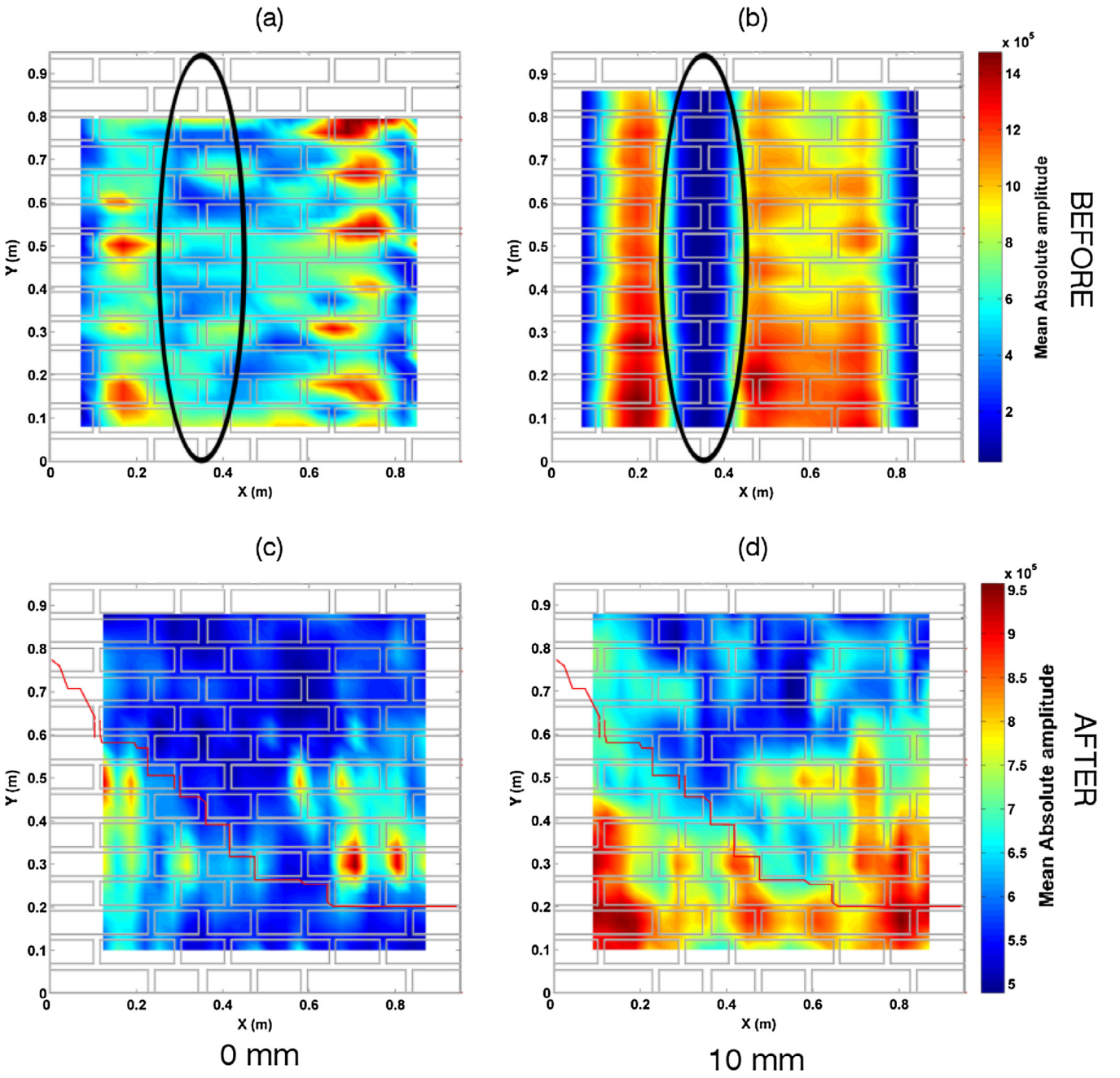

Fig. 18. Mean absolute amplitude calculated for the laboratory bricks sample before the load application, without (a) and with 10 mm of Plexiglas (b), and after the load application without (c) and with 10 mm of Plexiglas (d). The black ellipses indicate the location of the single row of bricks.

Lastly, ERT inverted models, represented in Fig. 19, substantiate the GPR results. We can see a rather heterogeneous undisturbed model, with a mean resistivity around 700 Ωm and a conductive zone (x = 0.15–0.3 m, resistivity ρ = 300 Ωm) due to the presence of the single row of bricks. After the load test the main fracture is clearly visible (ρ > 1000 Ωm). Therefore, also in this case high resistivity corresponds to high values of MAA and low values of dielectric constant.

4. Conclusions

In this paper, we present an application of the GPR and ERT methods for monitoring a load test executed on masonry samples, built up in the laboratory controlled conditions using tuff and bricks (widespread materials employed in Italy for decades for masonry buildings). The samples are reinforced with a conductive fibre fabric. Firstly we analysed the GPR response, due to the different construction materials and to the effect of the load application, through synthetic simulations with the additional goal to understand the benefit given by a dielectric layer, placed underneath the GPR antenna, for reconstruction of anomalies. The results demonstrated the capability of the method to detect the different geometry of the masonry sample (orientation of bricks, joints) and, after the load test, to clearly detect the fractures, even though the benefit of the Plexiglas layer was limited for acquisition made on the unreinforced face of the samples. The corresponding laboratory data display similar results, both in terms of detectability of anomalies and of the role played by the dielectric layer.

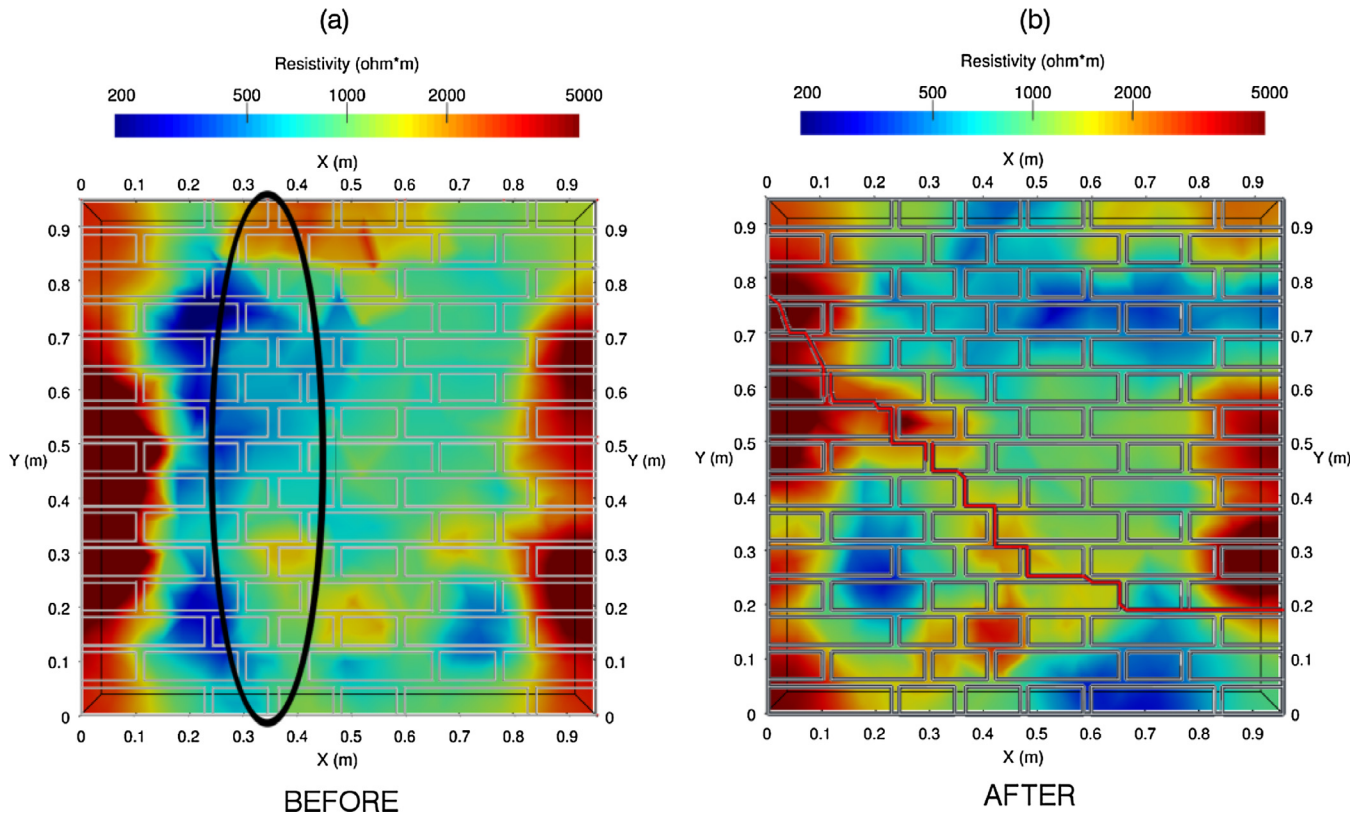

Fig. 19. ERT inverted model for bricks sample before (a) and after (b) load application. Horizontal slices are drawn at a depth of 50 ± 50 mm. The black ellipse indicates the location of the single row of bricks.

On the contrary, GPR laboratory data acquired directly on the reinforced face of samples, clearly demonstrate that using the dielectric layer can improve substantially the coupling and consequently the capability to detect fractures and to reach the rear face of the sample in the case of conductive materials, despite losing resolution. In this sense a further development of this research should involve a deeper analysis of the benefit of the Plexiglas interposition through theoretical and numerical studies. Therefore, this add-on, once specifically engineered and sized, will be easily implementable with a standard GPR system and will allow the investigation of high-conductive media (reinforcements, bars or with high moisture contents), in order to improve the detectability of hidden objects.

Mapping the GPR data in terms of the dielectric constant and mean absolute amplitude is particularly diagnostic to detect the effective fracturing pattern, after the application of the diagonal load. In fact we have lower dielectric constant together with higher amplitudes in presence of a high degree of fracturing. In addition to this, the capability to detect the fracturing pattern of the whole sample only using the standard GPR processing decreases as a function of the heterogeneity of the masonry, whereas small-sized elements (e.g. micro-fractures within the joints) can produce a high-scattering response leading to misunderstand the overall degree of fracturing of the sample. Consequently, for such cases the maps of dielectric constant and MAA can reduce the degree of uncertainty in the detection of the main fractures or, additionally, of voids and cavities. The ERT technique can be complementary used to validate the GPR evidence, where more resistive zones are associable with the presence of fractures and weakness zones. In fact, given the low resolution of the electrical method, it cannot be employed for these purposes as a standalone technique.

At the end, this paper demonstrated that the integrated application of GPR and ERT investigations can be a reliable tool to monitor static load tests, due to the complete non-invasiveness, the cost-effectiveness and the high-resolution achieved by these methods. Therefore, this procedure can be extended to whole load cycle (before, during and after the experiment), with the primary aim to have a quantitative assessment of the effective distribution of fractures within the sample during the load application.

Acknowledgments

The authors wish to thank Prof. Fabrizio Vestroni – Department of Structural and Geotechnical Engineering (DISG) of "Sapienza" University of Rome, for allowing us to perform geophysical measurements on the masonry samples.

Lucia Palladini (PhD student, "Sapienza" University of Rome) and Francesco Pugliese (laboratory technician, "Sapienza" University of Rome) are also thanked for their technical support in the laboratory.

References

[1] A. Adler, W.R. Lionheart, Uses and abuses of EIDORS: an extensible software base for EIT, Physiol. Meas. 27 (2006) S25.
[2] I.L. Al-Qadi, S. Lahouar, Measuring layer thicknesses with GPR–theory to practice, Constr. Build. Mater. 19 (10) (2005) 763–772.
[3] D. Arosio, J. Deparis, L. Zanzi, S. Garambois, Fracture characterization with GPR: a comparative study, in: Proceedings 16th International Conference on Ground Penetrating Radar, June 13–16, Hong Kong, 2016.
[4] ASTM E519, E519M-15, Standard Test Method for Diagonal Tension (Shear) in Masonry Assemblages 2015 ASTM International West Conshohocken, PA.
[5] V. Barrile, R. Pucinotti, Application of radar technology to reinforced concrete structures: a case study, NDT E Int. 38 (7) (2005) 596–604.
[6] A. Benedetto, F. Benedetto, Remote sensing of soil moisture content by GPR signal processing in the frequency domain, IEEE Sens. J. 10 (2011) 2432–2441.

[7] F. Benedetto, F. Tosti, GPR spectral analysis for clay content evaluation by the frequency shift method, J. Appl. Geophys. 97 (2013) 89–96.
[8] A. Benedetto, L. Pajewski, Civil Engineering Applications of Ground Penetrating Radar, Transactions in Civil and Environmental Engineering, Springer, Berlin, 2015, p. 371.
[9] L. Binda, L. Cantini, M. Lualdi, C. Tedeschi, A. Saisi, L. Zanzi, Investigation on structures and materials of the Castle of Avio (Trento, Italy), Adv. Archit. Ser. 20 (2005) 599–610.
[10] L. Binda, G. Cardani, L. Zanzi, Nondestructive testing evaluation of drying process in flooded full-scale masonry walls, ASCE J. Perform. Constr. Facil. 24 (5) (2010) 473–483.
[11] E. Cardarelli, G. De Donno, C. Scatigno, I. Oliveti, M.P. Martinez, N. Prieto-Taboada, Geophysical and geochemical techniques to assess the origin of rising damp of a Roman building (Ostia Antica archaeological site), Microchem. J. 2016 (129) (2010) 49–57.
[12] L.B. Conyers, Ground-Penetrating Radar for Archaeology, AltaMira Press, 258, 2013.
[13] D.J. Daniels, Ground Penetrating Radar, 2nd ed., IET, London, 2009, p. 734.
[14] P.J. D'Aranno, G. De Donno, M. Marsella, L. Orlando, B. Renzi, S. Salviani, M.L. Santarelli, S. Scifoni, A. Sonnessa, F. Verri, R. Volpe, High-resolution geomatic and geophysical techniques integrated with chemical analyses for the characterization of a Roman wall, J. Cultural Heritage 17 (1) (2016) 141–150.
[15] G. De Donno, 2D tomographic inversion of complex resistivity data on cylindrical models, Geophys. Prospect. 61 (Suppl. 1) (2013) 586–601.
[16] G. De Donno, E. Cardarelli, 3D complex resistivity tomography on cylindrical models using EIDORS, Near Surf. Geophys. 12 (5) (2014) 587–598.
[17] G. De Donno, E. Cardarelli, VEMI: a flexible interface for 3D tomographic inversion of time- and frequency-domain electrical data in EIDORS, Near Surf. Geophys. 15 (1) (2017) 43–58.
[18] C. Gaffney, Detecting trends in the prediction of the buried past: a review of geophysical techniques in archaeology, Archaeometry 50 (2008) 313–336.
[19] D. Goodman, Y. Nishimura, J.D. Rogers, GPR time slices in archaeological prospection, Archaeol. Prospection 2 (2) (1995) 85–90.
[20] D. Goodman, S. Piro, GPR Remote Sensing in Archaeology, Springer, Berlin, 2013, p. 233.
[21] G. Grandjean, J.C. Gourry, A. Bitri, Evaluation of GPR techniques for civil-engineering applications: study on a test site, J. Appl. Geophys. 45 (3) (2000) 141–156.
[22] K. Grote, S. Hubbard, J. Harvey, Y. Rubin, Evaluation of infiltration in layered pavements using surface GPR reflection techniques, J. Appl. Geophys. 57 (2) (2005) 129–153.
[23] L. Liu, J.W. Lane, Y. Quan, Radar attenuation tomography using the centroid frequency, J. Appl. Geophys. 40 (1) (1998) 105–116.
[24] H. Lorenzo, V. Cuéllar, M.C. Hernández, Close range radar remote sensing of concrete degradation in a textile factory floor, J. Appl. Geophys. 47 (3) (2001) 327–336.
[25] G. Marcari, M. Basili, F. Vestroni, Experimental investigation of tuff masonry samples reinforced with surface bonded basalt textile-reinforced mortar, Compos. B Eng. 108 (2017) 131–142.
[26] A. Martinez, A.P. Byrnes, Modeling Dielectric-constant Values of Geologic Materials: An Aid to Ground-penetrating Radar Data Collection and Interpretation, Kansas Geological Survey, University of Kansas, 2001.
[27] L. Mol, P.R. Preston, The writing's in the wall: a review of new preliminary applications of Electrical Resistivity Tomography within archaeology, Archaeometry 52 (6) (2010) 1079–1095.
[28] L. Orlando, E. Cardarelli, M. Cercato, G. De Donno, Characterization of a pre-trajan wall by integrated geophysical methods, Archaeol. Prospection 22 (3) (2015) 221–232.
[29] L. Orlando, E. Slob, Using multicomponent GPR to monitor cracks in a historical building, J. Appl. Geophys. 67 (4) (2009) 327–334.
[30] D. Pena, R. Feick, H.D. Hristov, W. Grote, Measurement and modeling of propagation losses in brick and concrete walls for the 900-MHz band, IEEE Trans. Antennas Propag. 51 (1) (2003) 31–39.
[31] M. Ramya, K. Balasubramaniam, M.S. Shunmugam, On a reliable assessment of the location and size of rebar in concrete structures from radargrams of ground-penetrating radar, Insight-Non-Destr. Test. Condition Monit. 58 (5) (2016) 264–270.
[32] O. Sass, H.A. Viles, Wetting and drying of masonry walls: 2D-resistivity monitoring of driving rain experiments on historic stonework in Oxford UK, J. Appl. Geophys. 70 (1) (2010) 72–83.
[33] K. Schulte, C. Baron, Load and failure analyses of CFRP laminates by means of electrical resistivity measurements, Compos. Sci. Technol. 36 (1) (1989) 63–76.
[34] A. Shaari, S.G. Millard, J.H. Bungey, Modelling the propagation of a radar signal through concrete as a low-pass filter, NDT E Int. 37 (3) (2004) 237–242.
[35] E. Slob, J. Fokkema, Coupling effects of two electric dipoles on an interface, Radio Sci. 37 (5) (2002) 1–10.
[36] R.H. Stolt, Migration by Fourier transform, Geophysics 43 (1) (1978) 23–48.
[37] P.I. Tsourlos, G.N. Tsokas, Non-destructive electrical resistivity tomography survey at the South Walls of the Acropolis of Athens, Archaeol. Prospection 18 (3) (2011) 173–186.
[38] C. Warren, A. Giannopoulos, I. Giannakis, gprMax: Open source software to simulate electromagnetic wave propagation for Ground Penetrating Radar, Comput. Phys. Commun. 209 (2016) 163–170.
[39] L. Zanzi, D. Arosio, Sensitivity and accuracy in rebar diameter measurements from dual-polarized GPR data, Constr. Build. Mater. 48 (2013) 1293–1301.